

1 **P wave anisotropy caused by partial eclogitization of descending crust demonstrated**
2 **by modelling effective petrophysical properties**

3 This is a non peer-reviewed preprint from earthArxiv, submitted to *Geochemistry, Geophysics,*
4 *Geosystems*
5

6 **Sascha Zertani^{1*}, Johannes C. Vrijmoed¹, Frederik Tilmann^{1,2}, Timm John^{1*}, Torgeir B.**
7 **Andersen³, & Loic Labrousse⁴**

8 ¹Institute of Geological Sciences, Freie Universität Berlin, 12249, Berlin, Germany.

9 ²Deutsches GeoForschungsZentrum, 14473, Potsdam, Germany.

10 ³The Centre of Earth Evolution and Dynamics (CEED), Department of Geosciences, University
11 of Oslo, 0316 Oslo, Norway.

12 ⁴Sorbonne Université, CNRS-INSU, Institut des Sciences de la Terre Paris, IStEP, UMR 7193,
13 F-75005 Paris, France.

14
15 Corresponding authors:

16 Sascha Zertani, Department of Geosciences, Freie Universität Berlin, Malteserstr. 74-100,
17 12249, Berlin, Germany. E-mail address: sascha.zertani@fu-berlin.de. Telephone: +49 30 838
18 75782.

19 and

20 Timm John, Department of Geosciences, Freie Universität Berlin, Malteserstr. 74-100, 12249,
21 Berlin, Germany. E-mail address: timm.john@fu-berlin.de. Telephone: +49 30 838 70103.

22 **Key Points:**

- 23 • Eclogitization of crustal rocks causes significant anisotropy on a crustal scale
- 24 • External geometric arrangement has no significant influence on effective seismic
25 properties
- 26 • Backazimuthal bias in receiver function studies can be caused by eclogitization

27

28 Abstract

29 Seismological studies of large-scale processes at convergent plate boundaries typically probe
30 lower crustal structures with wavelengths of several kilometers, whereas field-based studies
31 typically sample the resulting structures at a much smaller scale. To bridge this gap between
32 scales, we derive effective petrophysical properties on the 20-m, 100-m, and kilometer scales
33 based on numerical modelling with the Finite Element Method. Geometries representative of
34 eclogitization of crustal material are extracted from the partially eclogitized exposures on
35 Holsnøy (Norway). We find that the P wave velocity is controlled by the properties of the
36 lithologies rather than their geometric arrangement. P wave anisotropy, however, is dependent on
37 the fabric orientation of the associated rocks, as fabric variations cause changes in the orientation
38 of the initial anisotropy. As a result, different structural associations can result in effective
39 anisotropies ranging from ~0-4% for eclogites not associated with ductile deformation to up to
40 8% for those formed during ductile deformation. For the kilometer-scale structures, a scale that
41 in principle can be resolved by seismological studies, we obtained P wave velocities between 7.7
42 and 8.0 km s⁻¹. The effective P wave anisotropy on the kilometer-scale is ~3-4% and thus may
43 explain the backazimuthal dependence of seismological images of, for example, the Indian lower
44 crust currently underthrusting beneath the Himalaya. These results imply that seismic anisotropy
45 could be the key to visualize structures in active subduction and collision zones that are currently
46 invisible to geophysical methods and thus can be used to unravel the underlying processes active
47 at depth.

48

49 1. Introduction

50 Convergent plate boundaries are among the most important sites of crustal reorganization and
51 element recycling. There, crustal material is buried to great depths, recycled into the mantle,
52 integrated into orogenic roots and in some cases also exhumed back to the surface. All of these
53 processes result in the modification of crustal rocks through metamorphism and brittle and/or
54 ductile deformation. However, this occurs at depths inaccessible to direct observation. Thus,
55 such structures are either studied by geophysical imaging methods or by investigating exhumed
56 rocks that have been metamorphosed and/or deformed in the past (e.g., Austrheim, 1987;
57 Rondenay et al., 2008). Field-based studies of deep processes are restricted to rare exposures
58 where mineral assemblages and structures are not substantially overprinted during exhumation
59 (e.g., Austrheim, 1987; John & Schenk, 2003). In order to properly interpret seismic velocities
60 and deduce the ongoing metamorphic processes associated with large-scale tectonics we require

61 knowledge of how seismic properties change with depth and lithology (e.g., Kind et al., 2012;
62 Rondenay et al., 2008).

63 While field-based studies include information down to the micron scale, geophysical imaging
64 techniques employ wavelengths that are only sensitive to kilometer-scale structures (e.g., Bloch
65 et al., 2018; Kim et al., 2019). In addition, the resolution of geophysical imaging is often further
66 limited by the available station coverage and distribution of signal sources. This creates a large
67 gap between the scale at which we image structures with geophysical methods and the scale at
68 which we can observe structures in the field. Subsequently, seismic velocities that are measured
69 in the laboratory or calculated for individual samples may not be representative of the properties
70 of lithological and structural associations on a larger scale. As these structures are smaller than
71 the resolution of seismological methods the properties of the different constituents will act
72 together as one effective medium (e.g., Backus, 1962; Hudson, 1981; Okaya et al. 2019).

73 Specifically, eclogitization processes occurring at depth remain difficult to assess, although they
74 are suspected to play a major role in geodynamic processes (Austrheim, 1991; Dewey et al.,
75 1993; Yamato et al., 2019). Eclogitization causes a density increase of crustal material that
76 decreases buoyancy forces and significantly adds to driving forces (e.g., slab pull) at convergent
77 plate boundaries (e.g., Hetényi et al., 2007; Klemd et al., 2011). However, the same density
78 increase also significantly complicates the detection of eclogites at depth as it is combined with
79 an increase of the elastic moduli of the rock. Subsequently, the resulting seismic properties of
80 eclogites become similar to those of mantle peridotites. This makes distinction between the
81 mantle and crust at depth difficult (e.g., Bostock, 2013; Hetényi et al., 2007; Rondenay et al.,
82 2008; Yuan et al., 2000). Nevertheless, partially eclogitized material within a subducting slab
83 shows a range of geometric configurations and orientations of anisotropy in the constituent

84 lithologies, depending on conditions during formation (John & Schenk, 2003; Scambelluri et al.,
85 1995; Zertani et al., 2019b). It is therefore not necessarily straightforward to transform a
86 measured velocity into a degree of eclogitization.

87 Eclogites formed from dismembered parts of the subducting crust, for example at the plate
88 interface, often occur as undeformed boudins in a weaker matrix, typically composed of
89 metasediments (e.g., Hetzel et al., 1998; Pleuger et al., 2005) or serpentinites (e.g., Scambelluri
90 et al., 1995). On the other hand, field-based studies have shown that intra-slab eclogitization of
91 crustal rocks is often associated with fluid availability that enhances mineral reactions and
92 ductile deformation, first forming centimeter-thick shear zones (Austrheim, 1987; John &
93 Schenk, 2003). As eclogitization and deformation progress, such shear zones can widen and
94 connect into larger shear zone networks surrounding low-strain domains (e.g., Jolivet et al.,
95 2005) and the shear zones can ultimately reach a thickness of a few hundred meters (Angiboust
96 et al., 2011; Boundy et al., 1997; Raimbourg et al., 2005; Zertani et al., 2019b). In exposed
97 examples of coherent pieces of partially eclogitized crust, the preserved shear zones rarely reach
98 scales that can be resolved with geophysical methods and the complex associations would thus
99 act as an effective medium at depth (e.g., Zertani et al., 2019a).

100 In contrast, geophysical imaging methods are used to study large-scale processes active at great
101 depth in collision and subduction zones (e.g., Halpaap et al., 2018). To unravel structures caused
102 by metamorphism coeval with deformation, the receiver function method is of specific interest. It
103 is based on the conversion of P to S waves and vice versa at boundaries with contrasting
104 impedance and therefore mostly sensitive to structural boundaries (Kind et al., 2012). For
105 example, Schneider et al. (2013) imaged a low velocity zone below the Pamir corresponding to
106 the subducting lower continental crust of the Eurasian Plate. The velocity contrast of this zone

107 with respect to the surrounding mantle, however, decreases below a depth of ~100 km,
108 suggesting eclogitization of the down going crust. Nabelek et al. (2009) and Schulte-Pelkum et
109 al. (2005) observed a backazimuthal dependence of the retrieved signal in the lower crust of
110 India beneath the Himalaya that suggests a significant large-scale anisotropic fabric within the
111 lower continental crust of India.

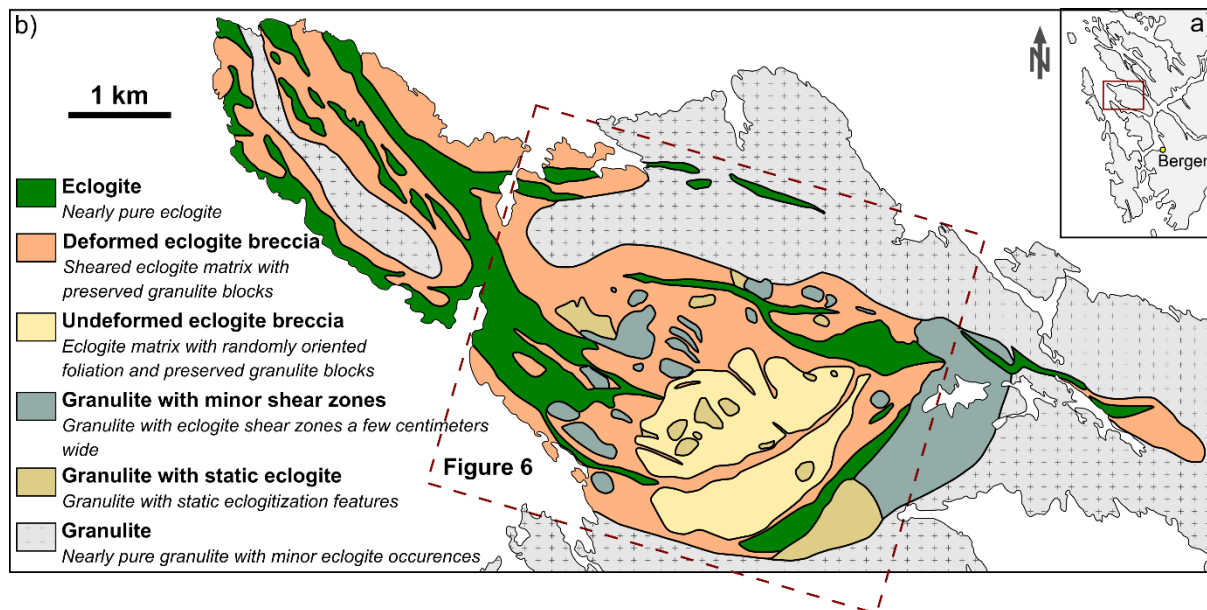
112 Direct estimates of seismic velocities are usually derived from samples that are only a few
113 centimeters in size (e.g., Kern et al., 1996) and extrapolation to scales that are resolvable using
114 geophysical methods relies on poorly supported assumptions, mainly that the composition of the
115 samples is representative of the crust at geophysically relevant scales and that the large-scale
116 organization of lithologies has no relevance. Voigt-Reuss-Hill averaging is the standard method
117 to calculate velocities within a medium based on the abundance of individual mineral phases
118 resulting in an average (isotropic) seismic velocity (Hill, 1952). The classic Backus averaging
119 allows calculation of the effective anisotropy of a finely layered medium. It is valid under the
120 assumption that the thickness of individual layers is far smaller than the seismic wavelength
121 (Backus, 1962). Although such averaging schemes are widely used to constrain seismic
122 velocities of various rocks, their capabilities are limited because they are only valid for simple
123 geometries that generally do not capture the structural complexity of real rocks.

124 To assess these simplifying assumptions, it is necessary to utilize a more sophisticated approach.
125 As a first step in this direction, we focus on the calculation of effective P wave velocities of
126 eclogite-facies associations using a technique based on stress calculations, for a variety of
127 representative geometries. The simplified geometries are derived from field observations on the
128 island of Holsnøy in the Bergen Arcs (Norway), where a >70 km² large complex of partially

129 eclogitized lower continental crust is exposed that provides an excellent coherent laboratory to
 130 study the geometries that are established during eclogitization.

131 2. Geological Setting

132 The exposed lower continental crust on the island of Holsnøy (Bergen Arcs, western Norway)
 133 has been partially eclogitized during the Caledonian orogeny (Austrheim, 1991). The rocks
 134 belong to the Lindås nappe, which together with the Dalsfjord and Jotun nappe complexes
 135 represents the lower crust of the former Jotun microcontinent that constituted part of the pre-
 136 Caledonian hyperextended margin of Baltica (Andersen et al., 2012; Jakob et al., 2019). The
 137 Lindås nappe is for a large part composed of anorthositic granulites that experienced Proterozoic
 138 granulite-facies P-T conditions of ~ 1 GPa and ~ 800 °C, at ~ 950 Ma (Austrheim & Griffin,
 139 1985). The P-T conditions in the following ~ 500 M.y. are unclear. The rocks, however, show no
 140 signs of significant alteration before the Scandian Caledonian collision and likely cooled to
 141 conditions reflecting mid to lower crustal conditions (Jamtveit et al., 1990).



142

143 **Fig. 1. Geological map of northwestern Holsnøy (modified from Jolivet et al. (2005) and Zertani et**
 144 **al. (2019b)). The inset (a) shows the location of Holsnøy in western Norway.**

145

146 During the Caledonian collision the Jotun microcontinent constituted the leading edge of Baltica,
147 which was integrated into the collision wedge as the lower plate (Corfu et al., 2014).
148 Subsequently, the Lindås nappe was subjected to peak eclogite-facies conditions of ~2 GPa and
149 ~750 °C at 429 Ma (Bhowany et al., 2018; Glodny et al., 2008; Jamtveit et al., 1990; Zhong et
150 al., 2019). Large volumes of the dry granulite-facies rocks, however, remained metastable and
151 were thus preserved (Austrheim, 1987; Jackson et al., 2004). Eclogitization is linked to fluid
152 availability and was facilitated along shear zones but also progressed into the rock volume as a
153 static overprint (Austrheim, 1987; Zertani et al., 2019b). Fluid infiltration was likely initiated via
154 brittle fractures, which provided fluid pathways within an otherwise dry rock (Austrheim, 1990;
155 Jamtveit et al., 1990).

156 This heterogeneously distributed transformation resulted in a complex mixture of eclogites and
157 granulites (Fig. 1). The resulting lithologies can be divided into six categories based on the
158 abundance of eclogite and the associated structural relationships (Boundy et al., 1992; Zertani et
159 al., 2019b). Next to the mostly unaltered granulite (<20% eclogite), small-scale eclogitization
160 features are distinguished into granulites cut by eclogite-facies shear zones a few centimeters
161 wide and granulites with eclogitized patches that are not associated with ductile deformation
162 (both 20-50% eclogite). With progressive eclogitization these evolve into the so-called eclogite
163 breccia, which can be described by two endmembers: sheared eclogite breccia composed of a
164 strongly sheared eclogite matrix containing preserved granulite blocks and unsheared eclogite
165 breccia, where the eclogite matrix was not subjected to pervasive ductile deformation (50-90%
166 eclogite). Ultimately, shear zones evolve that are up to a few hundred meters thick and are
167 almost entirely composed of eclogite with little to no preserved granulite (>90% eclogite).

168 **3. Model Setup**

169 **3.1 Finite element calculations**

170 The aim of this study is to obtain effective P wave velocities and the corresponding P wave
 171 anisotropy from variably eclogitized lower crustal rocks based on observed 2D geometric
 172 arrangements that act as an effective medium. The information extracted in the field is simplified
 173 and translated into numerical models with the goal of capturing the most essential properties of
 174 the observed field relationships. As the field observations along approximately planar exposures
 175 would require the introduction of essentially arbitrary additional parameters to create plausible
 176 three-dimensional models, this contribution focuses on 2D numerical modelling. Whereas this
 177 approach inevitably results in some differences in the inferred seismic velocities (compared to
 178 what would be obtained for the unknown true three-dimensional structure, the 2D models
 179 nevertheless are expected to provide a good approximation and therefore enhance our
 180 understanding of how geometries affect petrophysical properties from the outcrop to the map
 181 scale. It has to be noted that here we focus on P waves, as in our formulation the out-of-plane
 182 polarization of S waves is not included.

183 Both the effective medium and the individual rock types are treated as linear elastic anisotropic
 184 material for which Hooke's law gives the relationship between stress (σ_{ij}) and strain (ϵ_{kl}):

$$185 \quad \sigma_{ij} = c_{ijkl} \epsilon_{kl}$$

186 In 2D the $2 \times 2 \times 2 \times 2$ elastic tensor, which we represent by a symmetric 3-by-3 matrix in Voigt
 187 notation (using the mapping $11 \rightarrow 1$, $22 \rightarrow 2$ and $12 \rightarrow 3$), is sufficient to fully describe the in-plane
 188 anisotropy:

$$189 \quad \begin{bmatrix} c_{11} & c_{12} & c_{13} \\ c_{21} & c_{22} & c_{23} \\ c_{31} & c_{32} & c_{33} \end{bmatrix}$$

190 Due to symmetry considerations c_{13} , c_{23} , c_{31} , and c_{32} are expected to be zero, and c_{12} should be
 191 equal to c_{21} . One way of obtaining the effective properties is to run numerical experiments

192 solving the elasto-dynamic wave equations and recording the time necessary for a wave to travel
 193 through the medium (e.g., Saenger et al., 2004). Other studies have used asymptotic expansion
 194 homogenization to calculate the effect of mineral orientation on seismic anisotropy solving for
 195 the 6x6 elastic tensor in 3D (Naus-Thijssen et al., 2011a; 2011b; Vel et al., 2016). Alternatively,
 196 we calculate the P wave velocities from the elastic tensor of the effective medium using the
 197 formulas for transversely isotropic media (Mavko et al., 2009):

$$198 \quad V_p = (c_{11} \sin^2 \theta + c_{22} \cos^2 \theta + c_{33} + \sqrt{M})^{\frac{1}{2}} (2\rho)^{-1/2}$$

199 where:

$$200 \quad M = [(c_{11} - c_{33}) \sin^2 \theta - (c_{22} - c_{33}) \cos^2 \theta]^2 + (c_{12} - c_{33})^2 \sin^2 2\theta$$

201 The equations fully describe the P wave velocity in 2D because our calculations assume no out-
 202 of-plane properties, i.e., plane strain. Thus, the reduction of a transversely isotropic medium to
 203 2D, with the symmetry axis within the plane results in an anisotropic medium and is sufficient to
 204 describe the anisotropic elastic properties in 2D. The individual components of the 2D elastic
 205 tensor (c_{ijkl}) of the effective medium are calculated from the stresses and strains calculated in a
 206 set of numerical experiments. For this purpose, three experiments (Fig. 2) are performed for each
 207 geometric model, applying different boundary conditions: (1) The area of interest is compressed
 208 along the y axis along the upper and lower boundary by imposing a fixed displacement. Along
 209 the left and right boundary displacement in x direction is zero. (2) The medium is compressed
 210 horizontally, that is, along the x axis. In this case displacement in y direction is zero along the
 211 top and bottom boundary. (3) Finally, simple shear is enforced along the top and bottom
 212 boundary, that is, displacement to the right along the top boundary and to the left at the bottom
 213 boundary, resulting in shear parallel to the x axis. A fourth experiment (simple shear parallel to

214 the y axis) was used for validation and yielded the same results as experiment (3), as is required
 215 from the symmetry of the elasticity tensor.

216 The three experiments result in a set of nine equations for six unknown components of the stress
 217 tensor, so only 6 of these equations are needed. Due to the setup of each experiment specific
 218 strains are zero which allows to simplify the equations to:

$$219 \quad c_{21} = \frac{\sigma_{xx}}{\varepsilon_{yy}}, c_{22} = \frac{\sigma_{yy}}{\varepsilon_{yy}}, \text{ and } c_{23} = \frac{\sigma_{xy}}{\varepsilon_{yy}}$$

220 for experiment 1,

$$221 \quad c_{11} = \frac{\sigma_{xx}}{\varepsilon_{xx}}, c_{12} = \frac{\sigma_{yy}}{\varepsilon_{xx}}, \text{ and } c_{13} = \frac{\sigma_{xy}}{\varepsilon_{xx}}$$

222 for experiment 2, and

$$223 \quad c_{31} = \frac{\sigma_{xx}}{\varepsilon_{xy}}, c_{32} = \frac{\sigma_{yy}}{\varepsilon_{xy}}, \text{ and } c_{33} = \frac{\sigma_{xy}}{\varepsilon_{xy}}$$

224 for experiment 3.

225 To extract the elastic properties of the effective medium, strain (ε_{kl}) and stress (σ_{ij}) are averaged
 226 across the domain. The boundaries at which the displacement for each of the experiments is
 227 enforced are kept far away from the medium of interest to avoid boundary effects. Strain and
 228 stress are then averaged only across the domain which constitutes the medium of interest (red in
 229 Fig. 2). In the 20-m scale models (Fig. 3a and b) both lithologies are in contact with the inner
 230 boundary in some cases. Here the eclogite was extended into the area between inner and outer
 231 boundary to avoid edge effects.

232 The P wave velocities of the effective medium can then be calculated from the resulting 2D
 233 elastic tensor. Bulk density is obtained by calculating the mean of the densities weighted by the
 234 area of the granulite and eclogite used for the calculation.

235 The calculations are performed using the Galerkin finite element method (FEM) employing an
 236 irregular triangular grid. Meshing is done with the mesh generator triangle (Shewchuk, 1996).

237 Each triangular element consists of six nodes in which the displacement field is calculated with
238 quadratic interpolation and Gauss quadrature integration at three points.

239 The method of obtaining the P wave velocity described above was tested and benchmarked using
240 an anisotropic layered medium, a problem for which an analytical solution exists (Backus, 1962).
241 Benchmarking was performed on a regular grid and reproduced the analytical solution within
242 machine level precision.

243 3.2 Properties of the implemented lithologies

244 The physical properties for each element representing the different material are given by the
245 elastic tensor of the corresponding lithology, i.e., granulite or eclogite. Representative elastic
246 tensors were calculated from the velocity measurements (x-z plane) in Zertani et al. (2019a).
247 Those measurements were performed on a true triaxial multi-anvil press using the ultrasonic
248 pulse transmission technique (Kern, 1978) with varying pressure and temperature between
249 ambient conditions and 600 MPa and 600 °C, respectively. From this data, each component can
250 be calculated separately except for C_{12} , as this would require information on the variation of
251 elastic wave speeds along oblique directions not available from laboratory measurements.
252 Therefore, we used the mean P wave velocity between the x and z axis to approximate the
253 velocity of a P wave travelling at a 45° angle to the foliation. This results in an almost elliptical
254 anisotropy with the ellipticity parameter η_{κ} (Brownlee et al., 2017; Kawakatsu, 2016) varying
255 between 0.97 and 1.03. Brownlee et al. (2017) have shown that off-axis anisotropy deviates
256 systematically from elliptical symmetry for rocks with high anisotropy. However, this effect is
257 most pronounced for rocks with high mica and/or quartz contents, which is not the case for the
258 Holsnøy samples shown in Zertani et al. (2019a). The assumption of near-elliptical anisotropy
259 made here is thus in agreement with the scaling laws of the off-axis anisotropy proposed by

260 Brownlee et al. (2017). In order to test the relative influence of the intrinsic properties of the
261 constituting lithologies and the geometries themselves, we used two different eclogites and two
262 different granulites (Tab. 1). Because the eclogites measured by Zertani et al. (2019a) were all
263 collected from the main shear zones exposed on Holsnøy, they all have a high P wave
264 anisotropy. In order to estimate effective properties for statically eclogitized areas, where the
265 eclogite would likely have a lower initial anisotropy, we assumed a lower velocity in x direction
266 for one of the samples (N-101 in Zertani et al., 2019a), thus giving a lower P wave anisotropy of
267 4%, which is in accordance with others reported from Holsnøy (Fountain et al., 1994).
268 Specifically, we chose to use the velocity measured at lower confining pressure (600 MPa). This
269 way, while the velocity is artificially reduced it is still a function of the existing mineral
270 assemblage.

271 The calculations feature four different categories of structural associations as they are evident
272 from the field (e.g., Austrheim 1987; Raimbourg et al. 2005; Zertani et al., 2019b): (1) granulite
273 with small-scale eclogite shear zones (20-m scale; Figure 3a), (2) granulite with patches of static
274 eclogitization (20-m scale; Figure 3b), (3) sheared eclogite breccia (100-m scale; Figure 3c), and
275 (4) unsheared eclogite breccia (100-m scale; Figure 3d). For each of the categories a series of
276 calculations was performed systematically varying the main configurations that can be observed
277 in the field. These are: a) abundance of eclogite (10-50% eclogite for 20-m scale and 50-90%
278 eclogite for 100-m scale), b) orientation of the main foliation of the constituting lithologies (Fig.
279 3, Fig. 4), and c) strength of the deformation fabric in the lithologies (static vs. dynamic
280 eclogitization; Zertani et al., 2019b). The orientation of the foliation used for the calculations is
281 given in Figure 3 (as sketches) and Figure 4, where XX means that the fast axis and thus the
282 foliation of the two lithologies are parallel and XY that they are perpendicular to each other. The

283 strength of the deformation fabric is also given in Figure 3 (in % anisotropy) and Figure 4 with
284 the notation: E,H – higher-anisotropy eclogite, E,L – lower-anisotropy eclogite, G,H – higher-
285 anisotropy granulite, and G,L – lower anisotropy granulite.

286 The choice of orientation of these lithologies is related to their structural setting. For the small-
287 scale eclogite shear zones the fast axis of the eclogite is oriented parallel to the shear zone and its
288 foliation as would be established during ductile shear (e.g., Bascou et al., 2001). The fast axis of
289 the granulite is oriented either parallel or perpendicular to the shear zone thus representing a
290 situation where the shear zones are established parallel to the foliation of the granulite or
291 perpendicular to it. On Holsnøy, both of these scenarios are present in the field, however, most
292 shear zones develop obliquely to the granulite-facies foliation. The two scenarios introduced into
293 the calculations are thus endmember representations of the chosen field example.

294 Patches of statically eclogitized material on the other hand typically develop parallel to the
295 granulite foliation. For those calculations the fast axis of the granulite and subsequently the
296 foliation is horizontal. The fast axis of the eclogite is either parallel to the granulite foliation as
297 typically observed in the field or perpendicular to it. We chose to include this case as field
298 observations suggest that static eclogitization features can also crosscut the granulite foliation,
299 specifically in cases where the abundance of eclogite is large enough for individual granulite
300 blocks to start moving independently. This setup thus also represents endmember scenarios.

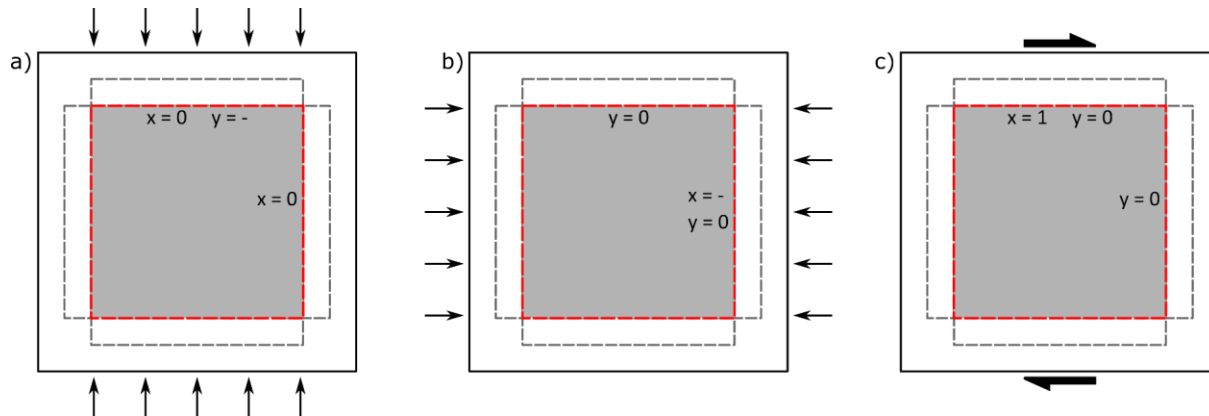
301 Finally, for the 100-m scale calculations of sheared and unsheared eclogite breccia the eclogite
302 foliation is horizontal in the models. For the sheared eclogite breccia this is straightforward,
303 representing the foliation formed during ductile shear. In the case of unsheared eclogite breccia
304 this was done to make comparison between the two easier. The granulite blocks in the sheared
305 case are often aligned nearly parallel to the eclogite foliation with their preserved internal

306 (granulite) foliation. However, rotation of these blocks is not always complete, and the granulite
 307 foliation can appear random in some cases. For the unsheared eclogite breccia the granulite
 308 blocks in the field can indeed have all possible orientations. Subsequently, the implemented
 309 orientations of the fast axis of granulite and eclogite also cover the endmember cases of what can
 310 be observed in the field.

311 **Tab. 1. Seismic velocities of the eclogites and granulites used for the FE calculations. The velocities**
 312 **(V_P and V_S), densities and anisotropies were taken from Zertani et al. (2019a). The star indicates**
 313 **that V_{PX} of N-101 was adjusted so that an anisotropy of 4% results (see text). Anisotropy was**
 314 **calculated as $100 \cdot (V_{PX} - V_{PY}) / V_{Pmean}$. Velocities (V) are given in km s^{-1} , density (ρ) in kg m^{-3} and**
 315 **anisotropy (A) in %.**

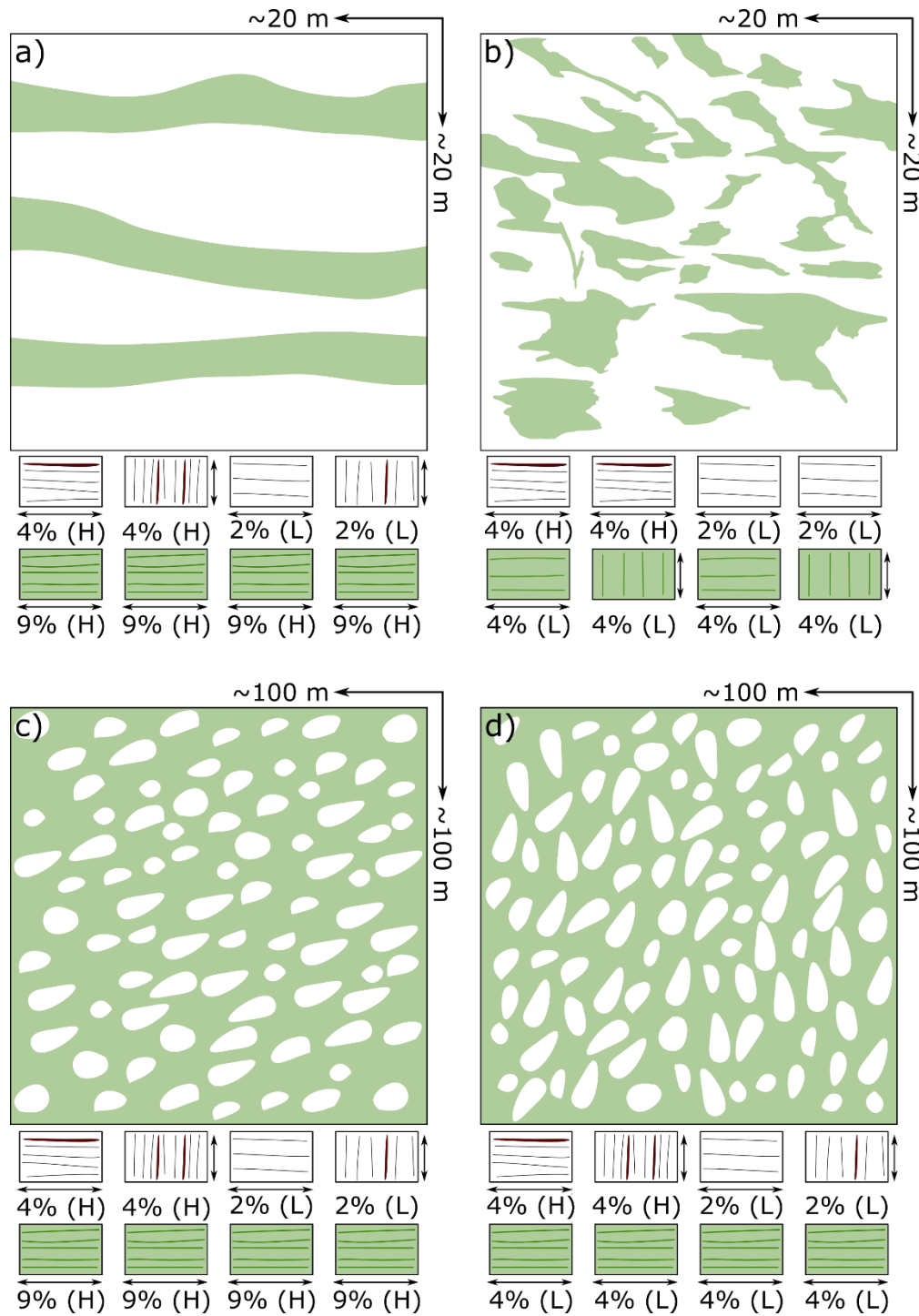
Sample	eclogite		granulite	
	N-059	N-101	N-058A	N-103
V_{PX}	8.45	8.31*	7.12	7.76
V_{PZ}	7.74	8.01	6.99	7.46
V_{S1}	4.58	4.65	3.75	4.12
V_{S2}	4.70	4.64	3.77	4.24
ρ	3296	3483	2833	3139
A_{VP}	9	4	2	4

316



317

318 **Fig. 2. Illustration of the three experiments with varying boundary conditions conducted for each**
 319 **computation; (a) Vertical compression, (b) horizontal compression, and (c) horizontal simple shear.**
 320 **The grey area represents the medium for which the properties are modelled. The red dotted square**
 321 **represents the boundaries surrounding the domain across which stress and strain are averaged and**
 322 **the grey dashed lines represents the area in which structures were extended if they are in direct**
 323 **contact with the boundary (see text for details).**



324

325 **Fig. 3. Examples of the geometries used for the FEM calculations. Eclogite is shown in green and**
 326 **granulite in white. (a) Small-scale eclogite facies shear zones representative of an area of ~20-by-20**
 327 **m. The example shown here contains ~30% eclogite. For the calculations with other eclogite**
 328 **abundances the thickness of the shear zone was varied accordingly. (b) Small-scale static eclogite**
 329 **overprint representative of an area of ~20-by-20 m. The example shown here contains ~30%**
 330 **eclogite. For calculations with other eclogite abundances the size of the eclogite patches was varied**
 331 **accordingly. (c) Sheared eclogite breccia with regularly oriented granulite blocks. The example is**

332 representative of an area of ~100-by-100 m and ~70% eclogite. The size of the granulite blocks
333 remains the same throughout all calculations. To perform calculations with different eclogite
334 abundances the abundance of granulite blocks was altered. (d) Unsheared eclogite breccia with the
335 same variations as in (c). Below each image the corresponding properties of eclogite and granulite
336 used for the calculations are given. Each column represents one model series. The percentage gives
337 the strength of the P wave anisotropy of the corresponding rock and the arrow gives the orientation
338 of the fast P wave direction used for the calculations. L and H indicate whether the higher or lower-
339 anisotropy version was used.

340
341 **Tab. 2. Resulting minimum and maximum P wave velocities and P wave anisotropy for each of the**
342 **calculated models. Velocities are given in km s^{-1} and anisotropy is given in %. For each model the**
343 **properties of the granulite and eclogite used for the calculation is indicated with the following**
344 **scheme; L: low-anisotropy, H: high-anisotropy, X: fast axis is oriented horizontally, and Y: fast axis**
345 **is oriented vertically.**

346

Structural Association	Eclogite	Granulite	Vp _{min}	Vp _{max}	A	Vp _{min}	Vp _{max}	A	Vp _{min}	Vp _{max}	A	Vp _{min}	Vp _{max}	A	Vp _{min}	Vp _{max}	A
<i>eclogite abundance [%]</i>																	
Granulite with small scale shear zones	H	X	H	X		7.49	7.84	4.6	7.52	7.92	5.3	7.54	7.98	5.7	7.56	8.04	6.2
	H	X	H	Y		7.58	7.76	2.3	7.67	7.75	1.1	7.72	7.78	0.9	7.74	7.87	1.7
	H	X	L	X		7.04	7.29	3.4	7.10	7.45	4.8	7.16	7.58	5.7	7.21	7.70	6.5
	H	X	L	Y		7.15	7.18	0.3	7.21	7.36	2.0	7.26	7.49	3.2	7.30	7.63	4.3
<i>eclogite abundance [%]</i>						10.9			20.0			31.9			38.2		47.5
Granulite with static eclogitization	L	X	H	X		7.51	7.81	3.9	7.55	7.86	4.0	7.61	7.92	4.0	7.64	7.96	4.2
	L	Y	H	X		7.54	7.78	3.2	7.60	7.80	2.6	7.69	7.83	1.8	7.73	7.85	1.5
	L	X	L	X		7.07	7.22	2.1	7.13	7.31	2.6	7.22	7.45	3.1	7.26	7.54	3.8
	L	Y	L	X		7.09	7.19	1.5	7.17	7.26	1.3	7.29	7.36	1.0	7.34	7.43	1.2
<i>eclogite abundance [%]</i>						53.1			63.1			75.0			81.5		89.2
Sheared eclogite breccia	H	X	H	X		7.60	8.11	6.5	7.63	8.18	7.0	7.66	8.26	7.6	7.68	8.31	7.9
	H	X	H	Y		7.75	7.95	2.6	7.75	8.06	4.0	7.74	8.18	5.5	7.74	8.25	6.3
	H	X	L	X		7.34	7.78	5.8	7.42	7.92	6.5	7.51	8.08	7.3	7.57	8.17	7.7
	H	X	L	Y		7.41	7.71	3.9	7.47	7.86	5.0	7.55	8.04	6.2	7.60	8.14	6.9
<i>eclogite abundance [%]</i>						52.5			63.2			70.8			81.7		90.3
Unsheared eclogite breccia	L	X	H	X		7.74	8.03	3.7	7.80	8.09	3.7	7.84	8.13	3.6	7.90	8.19	3.6
	L	X	H	Y		7.86	7.89	0.4	7.91	7.96	0.6	7.93	8.03	1.1	7.96	8.13	2.1
	L	X	L	X		7.48	7.65	2.2	7.59	7.78	2.5	7.68	7.87	2.5	7.80	8.03	2.9
	L	X	L	Y		7.55	7.57	0.6	7.65	7.72	1.0	7.72	7.82	1.3	7.82	7.99	2.1

348 **4. Results**

349

350 4.1 P wave velocity and anisotropy of small-scale eclogitization features

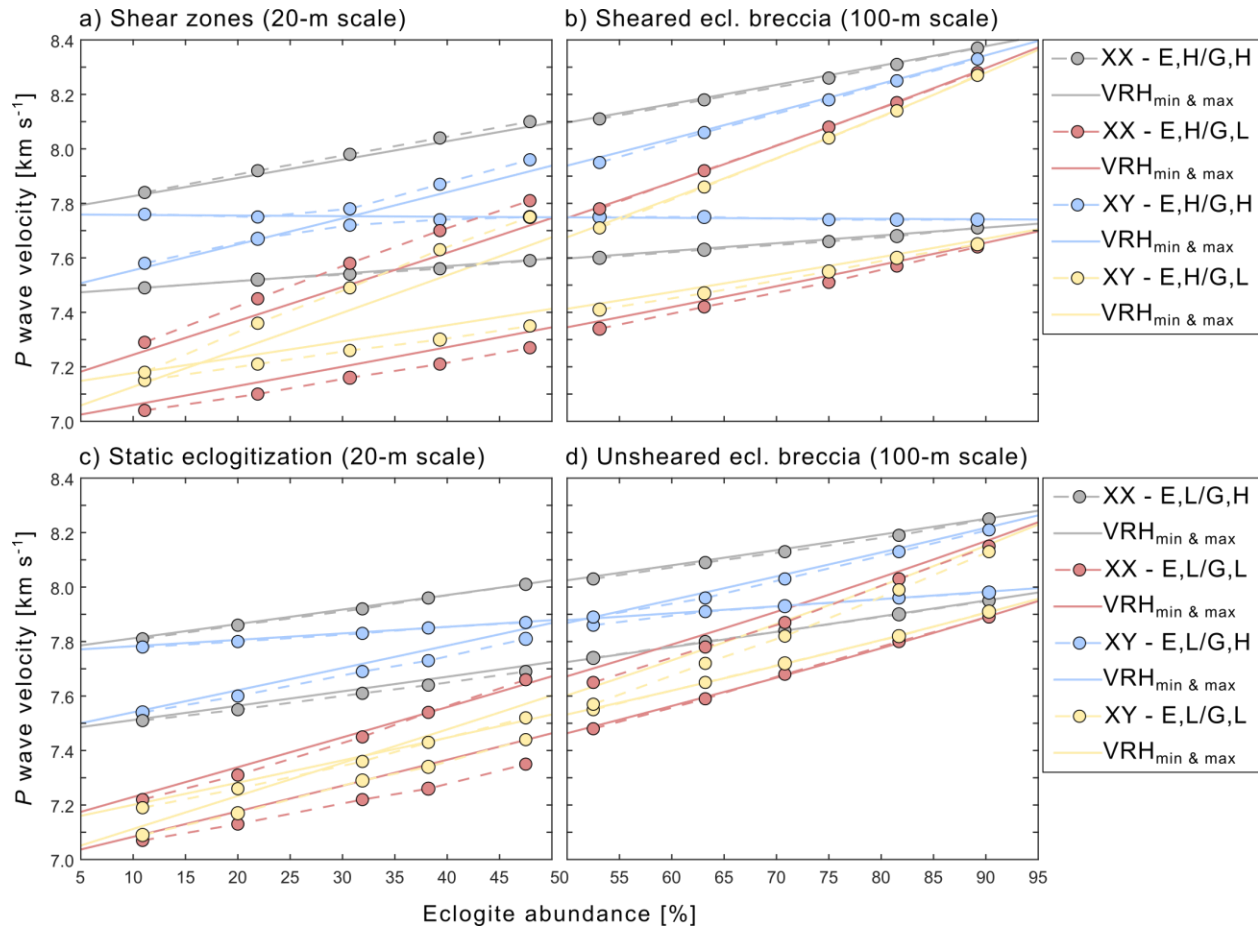
351 The process of eclogitization, as it can be studied on Holsnøy, is driven by two contrasting
352 endmember mechanisms: eclogitization proceeding along shear zones (Fig. 3a) or developing as a
353 static overprint (Fig. 3b). In the first type, eclogitization proceeds along shear zones that widen
354 progressively with time and a wide variety of shear zone thicknesses is found throughout the
355 field area (Austrheim, 1987). Hence, we calculated P wave velocities for 20 examples with
356 varying shear zone thickness as well as varying elastic properties of the eclogite and granulite
357 implemented in the models (Fig. 3, Tab. 2).

358 Comparing all models shows that the calculated P wave velocities with higher-anisotropy
359 (stronger deformation fabric) granulites are, in general, higher than those with lower-anisotropy
360 granulites. Furthermore, with increasing shear zone thickness (i.e., amount of eclogite), the P
361 wave velocity in both the slow and the fast P wave direction increases linearly (Tab. 2; Fig. 4a).
362 The one exception to this trend is given by the models that feature both higher-anisotropy
363 eclogite and the higher-anisotropy granulite, with the fast axis of both rocks oriented
364 perpendicular to each other: the fast axis of the eclogite parallel to the shear zones and the fast
365 axis of the granulite perpendicular to them. For this geometry, the resulting P wave velocities for
366 the fast and slow axis of the effective medium converge up to an eclogite abundance of ~30%
367 and then diverge toward higher eclogite abundance. This coincides with a change of the
368 orientations of the fast and slow direction. In this scenario, the velocity perpendicular to the
369 shear zones is almost constant. The velocity parallel to the shear zones, however, increases
370 significantly from 7.58 to 7.96 km s⁻¹ with increasing eclogite abundance. The fast axis is thus

371 perpendicular to the shear zones for an eclogite abundance <30% and parallel to the shear zones
372 from ~30–50% eclogite abundance. The orientation of the slow direction rotates progressively
373 away from the trend of the shear zones, i.e. toward the slow direction of the eclogite. In all other
374 model sequences, the fast direction is parallel to the shear zones and the slow direction is
375 perpendicular.

376 The corresponding P wave anisotropy also increases with increasing shear zone thickness and
377 reaches a maximum value of 7.1% (Fig. 5). In most models, this increase is near-linear with
378 increasing eclogite abundance. In contrast, the resulting P wave anisotropy of those calculations
379 featuring a higher-anisotropy granulite with the fast axis oriented perpendicular to the shear zone
380 decreases between ~10% and ~30% eclogite abundance and then increases until ~50% eclogite
381 abundance. Finally, the P wave anisotropy at ~50% eclogite abundance returns to approximately
382 the same value of ~2-3%, as the P wave anisotropy at ~10% eclogite abundance.

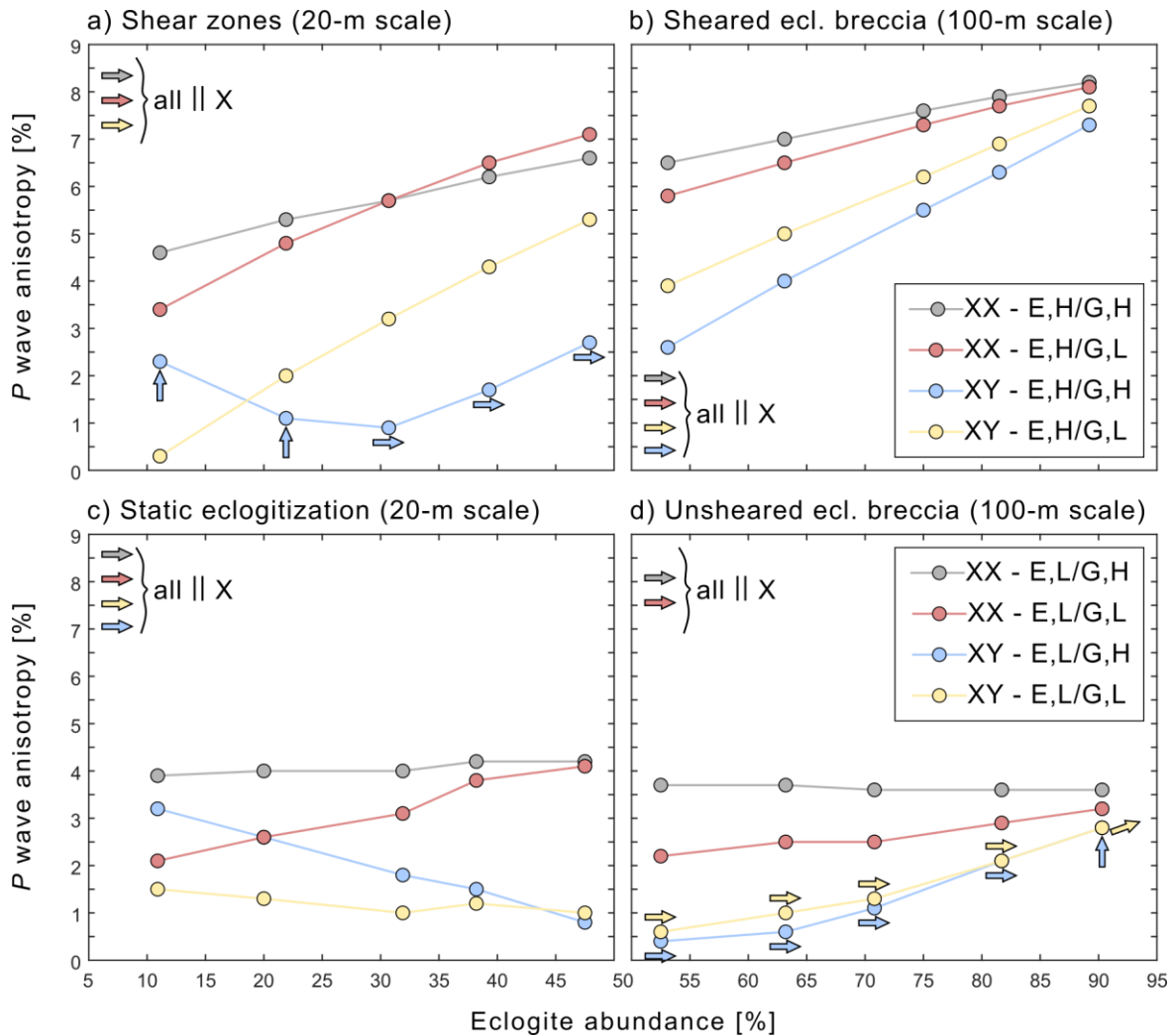
383 In general, the resulting P wave anisotropy is larger when the fast axes of both granulite and
384 eclogite are oriented parallel to the shear zone, compared to those examples where the fast axis
385 of the granulite is oriented perpendicular to the shear zone. At lower eclogite abundance the
386 calculations implementing a higher-anisotropy granulite result in a higher anisotropy of the
387 effective medium, while the results at higher eclogite abundance indicate that the anisotropy of
388 the effective medium is higher if the granulite has a lower intrinsic anisotropy (Fig. 5).



389

390 **Fig. 4. P wave velocities of the FEM calculations: (a) Small-scale eclogite shear zones, (b) sheared**
 391 **eclogite breccia, (c) small-scale static eclogite, and (d) unsheared eclogite breccia. The legend for (a)**
 392 **and (b) is to the right of (b) and the legend for (c) and (d) is to the right of (d). Each model series**
 393 **is shown by two connecting dashed lines. The upper line represents the maximum velocities and the**
 394 **lower line represents the minimum velocities. The legend is given in the following scheme; XX:**
 395 **foliation and fast axis of granulite and eclogite are parallel, XY: foliation and fast axis of granulite**
 396 **and eclogite are perpendicular (shown as sketches in Figure 3), E,H or E,L: eclogite with high**
 397 **anisotropy or low anisotropy, respectively, G,H or G,L: granulite with high or low anisotropy,**
 398 **respectively. Higher and lower anisotropy is indicated in % in Figure 3. Solid lines indicate Voigt-**
 399 **Reuss-Hill averages in the same color scheme as the modeling results averaged from the elastic**
 400 **tensor implemented in the corresponding calculations. Shown are calculated velocities parallel to x**
 401 **and y.**

402



403

404 **Fig. 5. P wave anisotropy of the FEM calculations: (a) Small-scale eclogite shear zones, (b) sheared**
 405 **eclogite breccia, (c) small-scale static eclogite, and (d) unsheared eclogite breccia. For a description**
 406 **of model types and explanation of the legend, refer to Fig. 4. Arrows indicate the direction of the**
 407 **fast axis of the effective medium with horizontal being in x direction and vertical in y direction.**

408

409 Additionally, eclogitization on Holsnøy also proceeded statically without significant ductile
 410 deformation (Jamtveit et al., 2000; Zertani et al., 2019b). Here, eclogitization most commonly
 411 advances parallel to the granulite foliation. For this case, we also calculated 20 different
 412 examples, varying both the abundance of eclogite and the elastic properties of the granulite and
 413 the eclogite (Fig. 3b; Tab. 2).

414 The resulting P wave velocities show a similar trend as those from the examples featuring small-
415 scale shear zones. Both the velocity of the fast and the slow axes increase linearly with
416 increasing abundance of eclogite (Fig. 4c). Further, the models featuring granulites with higher
417 anisotropy result in faster P wave velocities of the effective medium than the models
418 implementing lower-anisotropy granulites. Additionally, the P wave velocities are in the same
419 range as the ones calculated for small-scale shear zones.

420 The orientations of the fast and slow axes are typically constant with the fast axis being parallel
421 to the granulite foliation (horizontal) and the slow axis perpendicular. Only in the calculations
422 where the lower-anisotropy eclogite and granulite with the orientation of the fast axes
423 perpendicular to each other are implemented, the resulting orientation changes slightly. These
424 calculations indicate that the fast axis remains horizontal (i.e., parallel to the granulite foliation)
425 while the slow axis rotates slightly away from the initial vertical orientation.

426 The P wave anisotropy shows a variable trend comparing the different models. The medium
427 featuring the higher-anisotropy granulite, with both the fast axes of the granulite and eclogite
428 oriented parallel to each other result in a P wave anisotropy of ~4% that essentially does not
429 change with varying eclogite abundance (Fig. 5d). The same is observed for the models featuring
430 the lower-anisotropy granulite with the fast axes of the granulite and eclogite being oriented
431 perpendicular to each other. Here, the resulting P wave velocity remains relatively constant
432 around 1–2%.

433 In contrast, the resulting anisotropy of the other two model types changes with increasing
434 eclogite abundance. The sequence featuring a lower-anisotropy granulite with the fast axis
435 oriented parallel to the fast axis of the eclogite increases from ~2% to ~4%, while the sequence

436 featuring the higher-anisotropy granulite with the fast axes of the two rocks oriented
437 perpendicular to each other decreases from ~3% to <1%.

438 4.2 P-wave velocity of eclogite breccia

439 With increasing degree of eclogitization the so-called eclogite breccia develops, which is
440 composed of an eclogite matrix that surrounds preserved blocks of granulite (Boundy et al.,
441 1992). On Holsnøy, the eclogite breccia can be divided into two endmember types (Zertani et al.,
442 2019b): The sheared eclogite breccia is characterized by a strongly sheared and foliated eclogite
443 matrix, while the matrix of the unsheared eclogite breccia is diffuse and less foliated.

444 We calculated 20 examples for each of the two types, varying the abundance of eclogite and the
445 elastic properties of the granulite and eclogite (Fig. 3c, d; Tab. 2). For all examples of the sheared
446 eclogite breccia, the P wave velocities increase linearly with increasing eclogite abundance. All
447 fast axes and all slow axes converge toward higher eclogite abundances, thus giving fairly
448 distinct maximum and minimum P wave velocities at high eclogite abundances that are
449 independent of the elastic properties of the granulite implemented in the model. (Fig. 4; Fig. 5).

450 The slope of the linear increase for the different models is similar to the models dealing with
451 small-scale shear zones. Further, the fast axis of the effective medium in all models is parallel to
452 the shear plane (horizontal) and the slow axis is perpendicular. Additionally, the P wave
453 velocities at ~50% eclogite abundance agree well between the models for small-scale shear zones
454 and the sheared eclogite breccia at the same eclogite fraction.

455 As in the case of the small-scale shear zones, the P wave anisotropy calculated for the sheared
456 eclogite breccia increases nearly linearly with increasing eclogite abundance reaching 7–9% at
457 ~90%. Further, P wave anisotropy is consistently higher for models where the fast axes of the
458 granulite and the eclogite are oriented parallel. In this scenario the anisotropy reaches its

459 maximum when both the granulite and the eclogite have a high anisotropy. If the fast axis of the
460 granulite, however, is perpendicular to the fast axis of the eclogite, the resulting anisotropy is
461 higher when the implemented granulite has a lower anisotropy.

462 The P wave velocities calculated for the unsheared eclogite breccia show the same general trends
463 as those for the sheared eclogite breccia (Fig. 4d). The only deviation results from the examples
464 implementing granulite and eclogite with their anisotropy perpendicular to each other. Here the
465 calculations result in a change of the orientation at high eclogite abundances.

466 The trends of the P wave anisotropy of the unsheared eclogite breccia in all calculated examples
467 is lower than the comparable examples of the sheared eclogite breccia (Fig. 5). Most sequences,
468 however, also slightly increase with increasing eclogite abundance, except for those where a
469 lower-anisotropy eclogite is paired with the higher-anisotropy granulite, both of which have their
470 fast axes parallel to each other. In that case the P wave anisotropy is nearly constant at ~3.7%
471 (Tab. 2).

472 **5. Discussion**

473 Many studies have calculated or measured P wave velocities of various metamorphic rocks with
474 the aim of interpreting the results of large-scale geophysical imaging techniques (e.g., Almqvist
475 & Mainprice, 2017). However, the sample sizes used for these interpretations are typically far
476 below the resolution of geophysical studies. It is thus essential to understand how geometries
477 formed at depth during ongoing eclogitization shape the seismic properties of the effective
478 medium in combination with the (anisotropic) seismic properties of the constituent rocks.

479 We distinguish two geometrical contributing factors in order to characterize their influence
480 separately. (1) The configuration that the different lithologies have to one another on the outcrop
481 scale or larger. This includes, for example, eclogite shear zones that crosscut granulites. In the

482 following, this will be referred to as external geometry, as it involves the relationship of the
483 lithologies to each other but not specifically the properties of the constituting lithologies
484 themselves. (2) The second contributing geometrical factor will be referred to as internal
485 geometry. It highlights the properties of the lithologies themselves by characterizing the
486 relationship between the directional dependence of the elastic properties of the different
487 lithologies that is caused by, for example, crystallographic preferred orientations (CPO) or shape
488 preferred orientations (SPO). The internal geometry thus distinguishes whether the fastest
489 velocity of the eclogite and granulite are parallel or oblique to each other.

490 5.1 Effective properties of 20 m and 100 m scale structures

491 Essentially, the P wave velocities calculated for the different geometrical setups show that the
492 velocities are controlled by the velocities of the constituent rocks and their proportions (Fig. 4,
493 Fig. 5). This has been accepted and applied by previous studies by calculating, for example,
494 Voigt-Reuss-Hill (VRH) averages (Hill, 1952) and linking those with the CPOs of the mineral
495 phases (e.g., Hacker et al., 2014; Llana-Funez & Brown, 2012; Worthington et al., 2013). Most
496 of these studies, however, obtain information from the thin section scale to recognize crustal-
497 scale processes or to interpret the results from large-scale geophysical imaging studies. The
498 results presented in this study indicate that Voigt-Reuss-Hill averages calculated from outcrop-
499 scale features are sufficiently precise to estimate the effective properties on a variety of scales
500 (Fig. 4). Essentially, the external geometries that are representative of eclogitization of crustal
501 rocks have only limited influence on the resulting P wave velocities. Only in isolated cases the
502 velocities are modified, thus deviating from the calculated VRH averages (Fig. 4a and 4c). Here a
503 minor geometric effect is plausible, however, this effect results in a maximum modification of
504 $<0.2 \text{ km s}^{-1}$ of the P wave velocity and is thus negligible in the context of large-scale crustal

505 processes. In fact, most studies that distinguish between the effect of CPO vs. SPO on the thin
506 section scale conclude that the effect of SPO is negligible (e.g., Zhong et al., 2014), although
507 there is evidence that at least in the deep mantle SPO does produce seismic anisotropy (Faccenda
508 et al., 2019).

509 Furthermore, although Holsnøy serves as an example here, this observation can be transferred to
510 other exposures of partial eclogitization and is thus likely representative in more general terms.

511 The shear zones explored here, for example, constitute extreme cases of geometric arrangement
512 as shear zones are well ordered and have a significant lateral extent. It could thus be expected
513 that the influence of, for example, isolated eclogite boudins or blocks as reported from other
514 exposures (e.g., John & Schenk, 2003; Locatelli et al., 2019; Mørk, 1985) on effective P wave
515 velocities would be even smaller.

516 However, P wave anisotropy varies between the different geometrical configurations (Fig. 5). In
517 this context, our results reveal the importance of the internal geometry compared to that of the
518 external geometry (Fig. 4, Fig. 5). As discussed above, the external geometry only has a minor
519 effect on the P wave velocities and anisotropy of the effective medium. The variation of
520 anisotropy for the different configurations tested by us are thus controlled by the internal
521 geometry. The most important factor is the anisotropy of the constituent lithologies that are
522 necessary to produce significant anisotropy of the effective medium. Additionally, the effective
523 anisotropy is strengthened or weakened by the relationship of the individual anisotropies of the
524 lithologies. Anisotropies are higher if the fast axes of the lithologies are aligned but not higher
525 than the highest contributing anisotropy (Fig. 5). Further, our results demonstrate the
526 predominance of the higher-anisotropy lithology. The fast axis of the effective medium is
527 parallel to the anisotropy of the matrix lithology (i.e., in line with the fabric of granulite or

528 eclogite), if the difference in anisotropy between the lithologies is small, or parallel to the higher-
529 anisotropy lithology, even if this lithology is less abundant (Fig. 5). This means a strongly
530 deformed rock, such as eclogite in shear zones, controls the overall anisotropy even at low
531 abundances. The predominance of the higher-anisotropy phase has also been demonstrated on
532 the rock scale considering, for example, the alignment of mica (e.g., Naus-Thijssen, et al.,
533 2011b).

534 5.2 Effective properties on the kilometer scale

535 Combining our results with field observations provides the opportunity to understand how partial
536 eclogitization of crustal rocks alters the seismic properties on a scale significantly larger than
537 what can be measured in the laboratory. Our results suggest that P wave velocities are almost
538 entirely controlled by the velocities and abundances of the constituting rocks (Fig. 4). Essentially,
539 there is no difference in the P wave velocities between rocks that have formed through static
540 eclogitization and those that formed while undergoing ductile deformation. Neither the finite
541 geometries nor the intrinsic seismic anisotropy of the granulites and eclogites have a significant
542 impact on the resulting isotropic average bulk velocities and the variations that can be
543 distinguished are minor. The P wave anisotropy, however, is influenced strongly by the
544 anisotropy of the rocks that form the effective medium (Fig. 5). Further, our results show that the
545 rock with the higher anisotropy controls bulk anisotropy. In any case, the exemplary geometries
546 discussed above are still far smaller than what can be resolved with large-scale geophysical
547 methods.

548 Therefore, we used these results to extract bulk properties of the effective medium at a scale that
549 could be resolved by large-scale geophysical imaging (Fig. 6). Accordingly, we used an area on
550 Holsnøy that is ~3.9-by-4.6 km in size (Fig. 1 and Fig. 6a) and provides a coherent natural

551 laboratory for eclogitization related structures. The geometries are based on the map shown in
 552 Zertani et al. (2019b). As properties for the different map units we implemented the resulting
 553 elastic tensor of the examples shown above, choosing one representative example for each of the
 554 geometric configurations, i.e., sheared eclogite breccia at ~75% eclogite with the fast axis of
 555 higher-anisotropy eclogite and higher-anisotropy granulite parallel to each other and unsheared
 556 eclogite breccia at ~71% eclogite with the fast axis of the lower-anisotropy eclogite and the
 557 higher-anisotropy granulite parallel to each other (Tab. 2). For pure eclogite and granulite we
 558 chose the higher-anisotropy versions (Tab. 1) that were also used for the calculations discussed
 559 above (Zertani et al., 2019a). The elastic tensors were rotated so that the fast axis is parallel to
 560 the structures presented by Zertani et al. (2019b).

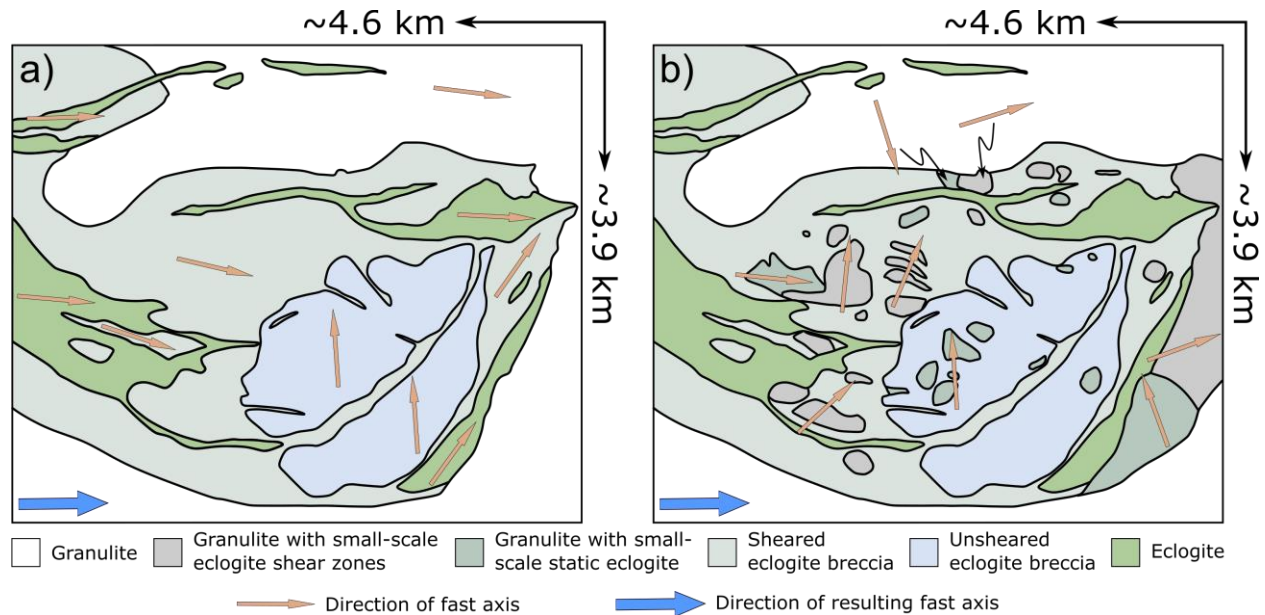


Fig. 6. Geometries used for the FEM calculations on the kilometer-scale. (a) Simpler model without smaller-scale structures. (b) More realistic model with small-scale structures. The location of this figure is given in Fig. 1. The yellow arrows indicate the direction of the fast axis implemented for the different lithologies. The blue arrows show the direction of the fastest velocity for each of the models.

Additionally, we implemented a second (more precise) model that also includes smaller-scale structures (Fig. 6b). Here we implemented the small-scale eclogite shear zones at ~31% eclogite

570 with the lower-anisotropy granulite and the higher-anisotropy eclogite (Tab. 2) and the small-
571 scale static eclogite at ~32% eclogite with the higher-anisotropy granulite and the lower-
572 anisotropy eclogite (Tab. 2).

573 The resulting P wave velocities of both models are in the range of 8.0 km s⁻¹ (fast axis) to 7.7 km
574 s⁻¹ (slow axis), i.e., within the expected range of the measured P wave velocities between
575 granulite and eclogite (Zertani et al., 2019a). Similar velocities are also reported from
576 geophysical studies dealing with active convergent settings, typically in the range of 7–8 km s⁻¹
577 (e.g., Nabelek et al., 2009; Schulte-Pelkum et al., 2005; Sippl et al., 2013). Additionally, our
578 calculation predicts a P wave anisotropy of 3.9% for the simpler model (Fig. 6a) and 3.3% for the
579 model that includes the small-scale structures (Fig. 6b). These values are in the range of what is
580 generally reported from eclogites and granulites (e.g., Brown et al., 2009; Worthington et al.,
581 2013). However, it has to be noted that the anisotropy presented here is representative for the
582 effective medium on a kilometer-scale and not only for single (handspecimen-sized) samples.

583 5.3 Implications for imaging of continental collision

584 The exposures on Holsnøy have been studied extensively because they provide a rare example to
585 study partial eclogitization of a coherent piece of continental crust (e.g., Austrheim 1987,
586 Bjørnerud et al., 2002; Jamtveit et al., 1990; 2000; Jolivet et al., 2005). These exposures are also
587 widely considered as representative of how crustal rocks transform to eclogites (e.g., Austrheim,
588 1990). Specifically, Holsnøy is often regarded as an ideal analog to the underplating crust of
589 India below the Himalaya (e.g., Jamtveit et al., 2019; Labrousse et al., 2010).

590 P wave velocities below the Tibetan plateau are suggested to be >7.0 km s⁻¹, which was
591 interpreted to represent ~30% eclogitization (Schulte-Pelkum et al., 2005). Our calculation for
592 Holsnøy is representative of ~50% eclogitization and yields slightly higher velocities. It thus

593 seems possible to estimate the degree of eclogitization based on P wave velocities. However, this
594 is only feasible if the backazimuthal distribution is sufficiently representative (Nabelek et al.,
595 2009; Schulte-Pelkum et al., 2005).

596 The retrieved P wave anisotropy of 3-4% from our model is sufficiently high that it could result
597 in a backazimuthal dependence of the retrieved signal in seismological studies. Additionally, our
598 calculations of P wave anisotropy of the different structural associations that could be expected
599 in a partially eclogitized crust show how different geometries can cause high P-wave anisotropy
600 (Fig. 5). In the Himalaya-Tibet collision system, where the lower crust of India is imaged below
601 the Himalaya (Jackson et al., 2004; Labrousse et al., 2010), using the receiver function method, it
602 has been shown that the retrieved signal of the Moho is sharp using earthquakes coming from the
603 north, while the Moho cannot be clearly imaged using earthquakes arriving from the south,
604 suggesting an anisotropic fabric within the buried crust (Nabelek et al., 2009; Schulte-Pelkum et
605 al., 2005). Nabelek et al. (2009) propose that this fabric is caused by the imbrication and rotation
606 of a stratified lower crust, excluding eclogites as the cause for the anisotropy because eclogites
607 typically have anisotropies <4%. However, our results show that partial eclogitization of the
608 lower crust does indeed produce considerable anisotropies at the scale sampled by geophysical
609 imaging techniques. Moreover, as shown by our results the effect of external geometry on
610 seismic anisotropy is limited suggesting that simple layering or imbrication might not produce
611 sufficient seismic anisotropy on this scale. Our results provide an alternative explanation for the
612 structures observed below the Himalaya. We suggest that considering the P wave velocities
613 reported and the backazimuthal dependence (Nabelek et al., 2009; Schulte-Pelkum et al., 2005)
614 eclogitization of the crust along ductile shear zones, similar to those exposed on Holsnøy seems
615 the more likely explanation.

616 Additionally, both kilometer-scale models we present here suggest that the fast axis of the shear
617 zone system is oriented WNW-ESE. At least in a qualitative sense this suggests that during
618 ongoing eclogitization, when this anisotropy was established it was dipping toward the upper
619 plate as is also evidenced by the top-east kinematics of the shear zone system (Jolivet et al.,
620 2005; Raimbourg et al., 2005). Geophysical imaging suggests a northward dipping fabric within
621 the lower Indian crust (Nabelek et al., 2009; Schulte-Pelkum et al., 2005), that is, dipping toward
622 the Asian plate, consistent with a top to the south shear sense. Our results demonstrate that
623 propagating eclogite-facies shear zones would produce a fabric and subsequent anisotropy with a
624 similar orientation. The scale of those shear zones is actually a minor issue, since our results
625 show the same dependence of effective medium properties on constitutive lithologies
626 independent of the scale.

627

628 5.4 Implications for oceanic subduction

629 Although the rocks on Holsnøy originate from continental crust some implications for oceanic
630 subduction settings can nevertheless be explored. In many geophysical studies of subducting
631 oceanic plates the descending crust is clearly imaged at shallow depth but loses its seismic signal
632 at greater depth (e.g., Bostock et al., 2002; Pearce et al., 2012; Rondenay et al., 2008; Yuan et
633 al., 2000). This decrease of the seismic signal is typically interpreted as due to a decreased
634 impedance contrast between descending crust and mantle rocks caused by eclogitization. This is
635 often accompanied by an increase of the dip angle in the Wadati-Benioff zone that indicates a
636 kink in the slab geometry (e.g., Halpaap et al., 2018; Klemd et al., 2011; Yuan et al., 2000).
637 While the subducting crust is invisible to seismological studies at this point its presence is
638 evidenced by the Wadati-Benioff zone and the inferred kink of the slab has been proposed as a

639 possible geometric obstacle that inhibits exhumation of crustal material subducted beyond that
640 point and is therefore potentially vital to understand subduction zone processes (Klemd et al.,
641 2011). Additionally, kinking on this scale must cause internal deformation of the subducting
642 slab. Whether or not this deformation is localized or homogeneously distributed and how this
643 deformation process affects ongoing eclogitization of the slab is enigmatic. However, utilizing
644 seismic anisotropy and the subsequent backazimuthal bias on the retrieved seismic signal might
645 prove a powerful tool to unravel these processes in active subduction zones. In this context,
646 although reliable imaging of the crustal anisotropy at these depths is still challenging, seismic
647 anisotropy of the subducted oceanic crust might make it possible to image it to larger depth and
648 illuminate an otherwise invisible slab.

649

650 **6. Conclusions**

651 We calculated P wave velocities and the corresponding P wave anisotropy for various
652 geometries, which are representative of partially eclogitized crust. The results show that dynamic
653 eclogitization, associated with shear zone formation, can cause a high P wave anisotropy that
654 increases with increasing eclogitization. The anisotropy of the effective medium is generally
655 controlled by the anisotropy of the matrix or by the contributing lithology that has the highest
656 anisotropy, even if this lithology is less abundant than the other contributors. Consequently,
657 patches of static eclogitization produce a comparatively low P wave anisotropy, which is in some
658 cases independent of the amount of eclogitization. The (external) geometric configuration of the
659 lithologies has little to no effect on the seismic properties of the effective medium.

660 Our results link partial eclogitization with geophysical observations at active convergent plate
661 boundaries. Previously, significant anisotropy due to eclogitization in deeply buried or subducted

662 crust has been excluded as eclogites are typically not strongly anisotropic. Contrary to this, our
663 results demonstrate that significant anisotropy due to partial eclogitization of crustal material on
664 a kilometer-scale is a likely explanation for the discrepancy of the signals retrieved from
665 different backazimuths in seismological studies. For example, the structures seen below the
666 Himalaya are likely anisotropic due to the formation of eclogite-facies shear zones within the
667 lower Indian crust. Additionally, our results strongly encourage the utilization of seismic
668 anisotropy as a tool to visualize the structural associations at depth, thus aiding the extraction of
669 the underlying mechanisms active during ongoing eclogitization of crustal material.

670

671 Acknowledgements

672 This research was supported by the Deutsche Forschungsgemeinschaft (DFG) in the framework
673 of the priority program SPP 2017 “Mountain Building in Four Dimensions (MB-4D)” by grant
674 JO 349/11-1. Funding for TBA was provided from Norges forskningsråd (NFR) project 250327.
675 We would like to thank Whitney Behr and one anonymous reviewer for their thorough and
676 thoughtful reviews and Maureen Long for editorial handling. Input data for the calculations are
677 provided as figures in the supporting information and will be uploaded to the OSF data
678 repository (osf.io) after acceptance.

679

680 References

- 681
682 Almqvist, B. S. G., & Mainprice, D. (2017). Seismic properties and anisotropy of the continental
683 crust: Predictions based on mineral texture and rock microstructure. *Reviews of*
684 *Geophysics*, 55(2), 367-433. <https://doi.org/10.1002/2016RG000552>
685 Andersen, T. B., Corfu, F., Labrousse, L., & Osmundsen, P.-T. (2012). Evidence for
686 hyperextension along the pre-Caledonian margin of Baltica. *Journal of the Geological*
687 *Society*, 169(5), 601-612. <https://doi.org/10.1144/0016-76492012-011>

- 688 Angiboust, S., Agard, P., Raimbourg, H., Yamato, P., & Huet, B. (2011). Subduction interface
689 processes recorded by eclogite-facies shear zones (Monviso, W. Alps). *Lithos*, *127*(1),
690 222-238. <https://doi.org/10.1016/j.lithos.2011.09.004>
- 691 Austrheim, H. (1987). Eclogitization of lower crustal granulites by fluid migration through shear
692 zones. *Earth and Planetary Science Letters*, *81*(2), 221-232.
693 [https://doi.org/10.1016/0012-821X\(87\)90158-0](https://doi.org/10.1016/0012-821X(87)90158-0)
- 694 Austrheim, H. (1990). The granulite-eclogite facies transition: A comparison of experimental
695 work and a natural occurrence in the Bergen Arcs, western Norway. *Lithos*, *25*(1), 163-
696 169. [https://doi.org/10.1016/0024-4937\(90\)90012-P](https://doi.org/10.1016/0024-4937(90)90012-P)
- 697 Austrheim, H. (1991). Eclogite formation and dynamics of crustal roots under continental
698 collision zones. *Terra Nova*, *3*(5), 492-499. [https://doi.org/10.1111/j.1365-
699 3121.1991.tb00184.x](https://doi.org/10.1111/j.1365-3121.1991.tb00184.x)
- 700 Austrheim, H., & Griffin, W. L. (1985). Shear deformation and eclogite formation within
701 granulite-facies anorthosites of the Bergen Arcs, western Norway. *Chemical Geology*,
702 *50*(1), 267-281. [https://doi.org/10.1016/0009-2541\(85\)90124-X](https://doi.org/10.1016/0009-2541(85)90124-X)
- 703 Backus, G. E. (1962). Long-wave elastic anisotropy produced by horizontal layering. *Journal of*
704 *Geophysical Research*, *67*(11), 4427-4440. <https://doi.org/10.1029/JZ067i011p04427>
- 705 Bascou, J., Barruol, G., Vauchez, A., Mainprice, D., & Egydio-Silva, M. (2001). EBSD-
706 measured lattice-preferred orientations and seismic properties of eclogites.
707 *Tectonophysics*, *342*(1), 61-80. [https://doi.org/10.1016/S0040-1951\(01\)00156-1](https://doi.org/10.1016/S0040-1951(01)00156-1)
- 708 Bhowany, K., Hand, M., Clark, C., Kelsey, D. E., Reddy, S. M., Pearce, M. A., et al. (2018).
709 Phase equilibria modelling constraints on P-T conditions during fluid catalysed
710 conversion of granulite to eclogite in the Bergen Arcs, Norway. *Journal of Metamorphic*
711 *Geology*, *36*(3), 315-342. <https://doi.org/10.1111/jmg.12294>
- 712 Bjørnerud, M. G., Austrheim, H., & Lund, M. G. (2002). Processes leading to eclogitization
713 (densification) of subducted and tectonically buried crust. *Journal of Geophysical*
714 *Research: Solid Earth*, *107*(B10), ETG 14-11-ETG 14-18.
715 <https://doi.org/10.1029/2001JB000527>
- 716 Bloch, W., John, T., Kummerow, J., Salazar, P., Krüger, O. S., & Shapiro, S. A. (2018).
717 Watching Dehydration: Seismic Indication for Transient Fluid Pathways in the Oceanic
718 Mantle of the Subducting Nazca Slab. *Geochemistry, Geophysics, Geosystems*, *19*, 3189-
719 3207. <https://doi.org/10.1029/2018GC007703>
- 720 Bostock, M., Hyndman, R., Rondenay, S., & Peacock, S. (2002). An inverted continental Moho
721 and serpentinization of the forearc mantle. *Nature*, *417*, 536-538.
722 <https://doi.org/10.1038/417536a>
- 723 Bostock, M. G. (2013). The Moho in subduction zones. *Tectonophysics*, *609*, 547-557.
724 <https://doi.org/10.1016/j.tecto.2012.07.007>
- 725 Boundy, T. M., Fountain, D. M., & Austrheim, H. (1992). Structural development and
726 petrofabrics of eclogite facies shear zones, Bergen Arcs, western Norway: implications
727 for deep crustal deformational processes. *Journal of Metamorphic Geology*, *10*(2), 127-
728 146. <https://doi.org/10.1111/j.1525-1314.1992.tb00075.x>
- 729 Boundy, T. M., Mezger, K., & Essene, E. J. (1997). Temporal and tectonic evolution of the
730 granulite-eclogite association from the Bergen Arcs, western Norway. *Lithos*, *39*(3), 159-
731 178. [https://doi.org/10.1016/S0024-4937\(96\)00026-6](https://doi.org/10.1016/S0024-4937(96)00026-6)
- 732 Brown, D., Llana-Funez, S., Carbonell, R., Alvarez-Marron, J., Marti, D., & Salisbury, M.
733 (2009). Laboratory measurements of P-wave and S-wave velocities across a surface

- 734 analog of the continental crust–mantle boundary: Cabo Ortegal, Spain. *Earth and*
735 *Planetary Science Letters*, 285(1-2), 27-38. <https://doi.org/10.1016/j.epsl.2009.05.032>
- 736 Brownlee, S. J., Schulte-Pelkum, V., Raju, A., Mahan, K., Condit, C., & Orlandini, O. F. (2017).
737 Characteristics of deep crustal seismic anisotropy from a compilation of rock elasticity
738 tensors and their expression in receiver functions. *Tectonics*, 36(9), 1835-1857.
739 <https://doi.org/10.1002/2017tc004625>
- 740 Corfu, F., Andersen, T. B., & Gasser, D. (2014). The Scandinavian Caledonides: main features,
741 conceptual advances and critical questions. *Geological Society, London, Special*
742 *Publications*, 390(1), 9-43. <https://doi.org/10.1144/sp390.25>
- 743 Dewey, J. F., Ryan, P. D., & Andersen, T. B. (1993). Orogenic uplift and collapse, crustal
744 thickness, fabrics and metamorphic phase changes: the role of eclogites. *Geological*
745 *Society, London, Special Publications*, 76(1), 325-343.
746 <https://doi.org/10.1144/GSL.SP.1993.076.01.16>
- 747 Faccenda, M., Ferreira, A. M. G., Tisato, N., Lithgow-Bertelloni, C., Stixrude, L., &
748 Pennacchioni, G. (2019). Extrinsic Elastic Anisotropy in a Compositionally
749 Heterogeneous Earth's Mantle. *Journal of Geophysical Research: Solid Earth*, 124, 1671-
750 1687. <https://doi.org/10.1029/2018JB016482>
- 751 Fountain, D. M., Boundy, T. M., Austrheim, H., & Rey, P. (1994). Eclogite-facies shear zones—
752 deep crustal reflectors? *Tectonophysics*, 232(1), 411-424. [https://doi.org/10.1016/0040-](https://doi.org/10.1016/0040-1951(94)90100-7)
753 [1951\(94\)90100-7](https://doi.org/10.1016/0040-1951(94)90100-7)
- 754 Glodny, J., Kühn, A., & Austrheim, H. (2008). Geochronology of fluid-induced eclogite and
755 amphibolite facies metamorphic reactions in a subduction–collision system, Bergen Arcs,
756 Norway. *Contributions to Mineralogy and Petrology*, 156(1), 27-48.
757 <https://doi.org/10.1007/s00410-007-0272-y>
- 758 Hacker, B., Ritzwoller, M., & Xie, J. (2014). Partially melted, mica-bearing crust in Central
759 Tibet. *Tectonics*, 33(7), 1408-1424. <https://doi.org/10.1002/2014TC003545>
- 760 Halpaap, F., Rondenay, S., & Ottemöller, L. (2018). Seismicity, Deformation, and
761 Metamorphism in the Western Hellenic Subduction Zone: New Constraints From
762 Tomography. *Journal of Geophysical Research: Solid Earth*, 123(4), 3000-3026.
763 <https://doi.org/10.1002/2017JB015154>
- 764 Hetényi, G., Cattin, R., Brunet, F., Bollinger, L., Vergne, J., Nábělek, J. L., & Diament, M.
765 (2007). Density distribution of the India plate beneath the Tibetan plateau: Geophysical
766 and petrological constraints on the kinetics of lower-crustal eclogitization. *Earth and*
767 *Planetary Science Letters*, 264(1-2), 226-244. <https://doi.org/10.1016/j.epsl.2007.09.036>
- 768 Hetzel, R., Echtler, H. P., Seifert, W., Schulte, B. A., & Ivanov, K. S. (1998). Subduction- and
769 exhumation-related fabrics in the Paleozoic high-pressure–low-temperature Maksyutov
770 Complex, Antingan area, southern Urals, Russia. *GSA Bulletin*, 110(7), 916-930.
771 [https://doi.org/10.1130/0016-7606\(1998\)110<0916:SAERFI>2.3.CO;2](https://doi.org/10.1130/0016-7606(1998)110<0916:SAERFI>2.3.CO;2)
- 772 Hill, R. (1952). The elastic behaviour of a crystalline aggregate. *Proceedings of the Physical*
773 *Society. Section A*, 65(5), 349-354.
- 774 Hudson, J. A. (1981). Wave speeds and attenuation of elastic waves in material containing
775 cracks. *Geophysical Journal International*, 64(1), 133-150.
776 <https://doi.org/10.1111/j.1365-246X.1981.tb02662.x>
- 777 Jackson, J. A., Austrheim, H., McKenzie, D., & Priestley, K. (2004). Metastability, mechanical
778 strength, and the support of mountain belts. *Geology*, 32(7), 625-628.
779 <https://doi.org/10.1130/g20397.1>

- 780 Jakob, J., Andersen, T. B., & Kjøll, H. J. (2019). A review and reinterpretation of the
781 architecture of the South and South-Central Scandinavian Caledonides—A magma-poor
782 to magma-rich transition and the significance of the reactivation of rift inherited
783 structures. *Earth-Science Reviews*, 192, 513-528.
784 <https://doi.org/10.1016/j.earscirev.2019.01.004>
- 785 Jamtveit, B., Austrheim, H., & Malthe-Sorensen, A. (2000). Accelerated hydration of the
786 Earth's deep crust induced by stress perturbations. *Nature*, 408(6808), 75-78.
787 <https://doi.org/10.1038/35040537>
- 788 Jamtveit, B., Bucher-Nurminen, K., & Austrheim, H. (1990). Fluid controlled eclogitization of
789 granulites in deep crustal shear zones, Bergen arcs, Western Norway. *Contributions to*
790 *Mineralogy and Petrology*, 104(2), 184-193. <https://doi.org/10.1007/bf00306442>
- 791 Jamtveit, B., Petley-Ragan, A., Incel, S., Dunkel, K. G., Aupart, C., Austrheim, H., et al. (2019).
792 The effects of earthquakes and fluids on the metamorphism of the lower continental crust.
793 *Journal of Geophysical Research: Solid Earth*, 124(8).
794 <https://doi.org/10.1029/2018jb016461>
- 795 John, T., & Schenk, V. (2003). Partial eclogitisation of gabbroic rocks in a late Precambrian
796 subduction zone (Zambia): prograde metamorphism triggered by fluid infiltration.
797 *Contributions to Mineralogy and Petrology*, 146(2), 174-191.
798 <https://doi.org/10.1007/s00410-003-0492-8>
- 799 Jolivet, L., Raimbourg, H., Labrousse, L., Avigad, D., Leroy, Y., Austrheim, H., & Andersen, T.
800 B. (2005). Softening triggered by eclogitization, the first step toward exhumation during
801 continental subduction. *Earth and Planetary Science Letters*, 237(3-4), 532-547.
802 <https://doi.org/10.1016/j.epsl.2005.06.047>
- 803 Kawakatsu, H. (2016). A new fifth parameter for transverse isotropy. *Geophysical Journal*
804 *International*, 204(1), 682-685. <https://doi.org/10.1093/gji/ggv479>
- 805 Kern, H. (1978). The effect of high temperature and high confining pressure on compressional
806 wave velocities in quartz-bearing and quartz-free igneous and metamorphic rocks.
807 *Tectonophysics*, 44(1), 185-203. [https://doi.org/10.1016/0040-1951\(78\)90070-7](https://doi.org/10.1016/0040-1951(78)90070-7)
- 808 Kern, H., Gao, S., & Liu, Q.-S. (1996). Seismic properties and densities of middle and lower
809 crustal rocks exposed along the North China Geoscience Transect. *Earth and Planetary*
810 *Science Letters*, 139(3), 439-455. [https://doi.org/10.1016/0012-821X\(95\)00240-D](https://doi.org/10.1016/0012-821X(95)00240-D)
- 811 Kim, D., Keranen, K. M., Abers, G. A., & Brown, L. D. (2019). Enhanced Resolution of the
812 Subducting Plate Interface in Central Alaska From Autocorrelation of Local Earthquake
813 Coda. *Journal of Geophysical Research: Solid Earth*, 124(2), 1583-1600.
814 <https://doi.org/10.1029/2018jb016167>
- 815 Kind, R., Yuan, X., & Kumar, P. (2012). Seismic receiver functions and the lithosphere–
816 asthenosphere boundary. *Tectonophysics*, 536-537, 25-43.
817 <https://doi.org/10.1016/j.tecto.2012.03.005>
- 818 Klemm, R., John, T., Scherer, E. E., Rondenay, S., & Gao, J. (2011). Changes in dip of subducted
819 slabs at depth: Petrological and geochronological evidence from HP–UHP rocks
820 (Tianshan, NW-China). *Earth and Planetary Science Letters*, 310(1-2), 9-20.
821 <https://doi.org/10.1016/j.epsl.2011.07.022>
- 822 Labrousse, L., Hetényi, G., Raimbourg, H., Jolivet, L., & Andersen, T. B. (2010). Initiation of
823 crustal-scale thrusts triggered by metamorphic reactions at depth: Insights from a
824 comparison between the Himalayas and Scandinavian Caledonides. *Tectonics*, 29(5),
825 TC5002. <https://doi.org/10.1029/2009TC002602>

- 826 Llana-Funez, S., & Brown, D. (2012). Contribution of crystallographic preferred orientation to
827 seismic anisotropy across a surface analog of the continental Moho at Cabo Ortegal,
828 Spain. *Geological Society of America Bulletin*, 124(9-10), 1495-1513.
829 <https://doi.org/10.1130/b30568.1>
- 830 Locatelli, M., Federico, L., Agard, P., & Verlaguet, A. (2019). Geology of the southern Monviso
831 metaophiolite complex (W-Alps, Italy). *Journal of Maps*, 15(2), 283-297.
832 <https://doi.org/10.1080/17445647.2019.1592030>
- 833 Mavko, G., Mukerji, T., & Dvorkin, J. (2009). *The rock physics handbook: Tools for seismic*
834 *analysis of porous media*: Cambridge university press.
- 835 Nabelek, J., Hetenyi, G., Vergne, J., Sapkota, S., Kafle, B., Jiang, M., et al. (2009). Underplating
836 in the Himalaya-Tibet collision zone revealed by the Hi-CLIMB experiment. *Science*,
837 325(5946), 1371-1374. <https://doi.org/10.1126/science.1167719>
- 838 Mørk, M. B. E. (1985). A gabbro to eclogite transition on Flemsøy, Sunnmøre, western Norway.
839 *Chemical Geology*, 50(1), 283-310. [https://doi.org/10.1016/0009-2541\(85\)90125-1](https://doi.org/10.1016/0009-2541(85)90125-1)
- 840 Naus-Thijssen, F. M. J., Goupee, A. J., Johnson, S. E., Vel, S. S., & Gerbi, C. (2011a). The
841 influence of crenulation cleavage development on the bulk elastic and seismic properties
842 of phyllosilicate-rich rocks. *Earth and Planetary Science Letters*, 311(3), 212-224.
843 <https://doi.org/10.1016/j.epsl.2011.08.048>
- 844 Naus-Thijssen, F. M. J., Goupee, A. J., Vel, S. S., & Johnson, S. E. (2011b). The influence of
845 microstructure on seismic wave speed anisotropy in the crust: computational analysis of
846 quartz-muscovite rocks. *Geophysical Journal International*, 185(2), 609-621.
847 <https://doi.org/10.1111/j.1365-246X.2011.04978.x>
- 848 Okaya, D., Vel, S. S., Song, W. J., & Johnson, S. E. (2019). Modification of crustal seismic
849 anisotropy by geological structures (“structural geometric anisotropy”). *Geosphere*,
850 15(1), 146-170. <https://doi.org/10.1130/GES01655.1>
- 851 Pearce, F. D., Rondenay, S., Sachpazi, M., Charalampakis, M., & Royden, L. H. (2012). Seismic
852 investigation of the transition from continental to oceanic subduction along the western
853 Hellenic Subduction Zone. *Journal of Geophysical Research: Solid Earth*, 117, B07306.
854 <https://doi.org/10.1029/2011JB009023>
- 855 Pleuger, J., Froitzheim, N., & Jansen, E. (2005). Folded continental and oceanic nappes on the
856 southern side of Monte Rosa (western Alps, Italy): Anatomy of a double collision suture.
857 *Tectonics*, 24(4). <https://doi.org/10.1029/2004TC001737>
- 858 Raimbourg, H., Jolivet, L., Labrousse, L., Leroy, Y., & Avigad, D. (2005). Kinematics of
859 syneclogite deformation in the Bergen Arcs, Norway: implications for exhumation
860 mechanisms. *Geological Society, London, Special Publications*, 243(1), 175-192.
861 <https://doi.org/10.1144/gsl.sp.2005.243.01.13>
- 862 Rondenay, S., Abers, G. A., & van Keken, P. E. (2008). Seismic imaging of subduction zone
863 metamorphism. *Geology*, 36(4), 275-278. <https://doi.org/10.1130/G24112A.1>
- 864 Saenger, E. H., Krüger, O. S., & Shapiro, S. A. (2004). Effective elastic properties of randomly
865 fractured soils: 3D numerical experiments. *Geophysical Prospecting*, 52(3), 183-195.
866 <https://doi.org/10.1111/j.1365-2478.2004.00407.x>
- 867 Scambelluri, M., Müntener, O., Hermann, J. r., Piccardo, G. B., & Trommsdorff, V. (1995).
868 Subduction of water into the mantle: History of an Alpine peridotite. *Geology*, 23(5),
869 459-462. [https://doi.org/10.1130/0091-7613\(1995\)023<0459:SOWITM>2.3.CO;2](https://doi.org/10.1130/0091-7613(1995)023<0459:SOWITM>2.3.CO;2)

- 870 Schneider, F. M., Yuan, X., Schurr, B., Mechie, J., Sippl, C., Haberland, C., et al. (2013).
871 Seismic imaging of subducting continental lower crust beneath the Pamir. *Earth and*
872 *Planetary Science Letters*, 375, 101-112. <https://doi.org/10.1016/j.epsl.2013.05.015>
- 873 Schulte-Pelkum, V., Monsalve, G., Sheehan, A., Pandey, M. R., Sapkota, S., Bilham, R., & Wu,
874 F. (2005). Imaging the Indian subcontinent beneath the Himalaya. *Nature*, 435(7046),
875 1222-1225. <https://doi.org/10.1038/nature03678>
- 876 Shewchuk, J. R. (1996). Triangle: Engineering a 2D quality mesh generator and Delaunay
877 triangulator. In M. C. Lin & D. Manocha (Eds.), *Applied Computational Geometry*
878 *Towards Geometric Engineering* (Vol. 1148, pp. 203-222). Berlin, Heidelberg: Springer
879 Berlin Heidelberg.
- 880 Sippl, C., Schurr, B., Tymphel, J., Angiboust, S., Mechie, J., Yuan, X., et al. (2013). Deep burial
881 of Asian continental crust beneath the Pamir imaged with local earthquake tomography.
882 *Earth and Planetary Science Letters*, 384, 165-177.
883 <https://doi.org/10.1016/j.epsl.2013.10.013>
- 884 Vel, S. S., Cook, A. C., Johnson, S. E., & Gerbi, C. (2016). Computational homogenization and
885 micromechanical analysis of textured polycrystalline materials. *Computer Methods in*
886 *Applied Mechanics and Engineering*, 310, 749-779.
887 <https://doi.org/10.1016/j.cma.2016.07.037>
- 888 Worthington, J. R., Hacker, B. R., & Zandt, G. (2013). Distinguishing eclogite from peridotite:
889 EBSD-based calculations of seismic velocities. *Geophysical Journal International*,
890 193(1), 489-505. <https://doi.org/10.1093/gji/ggt004>
- 891 Yamato, P., Duretz, T., & Angiboust, S. (2019). Brittle/ductile deformation of eclogites: insights
892 from numerical models. *Geochemistry, Geophysics, Geosystems*, 20, 3116–3133.
893 <https://doi.org/10.1029/2019gc008249>
- 894 Yuan, X., Sobolev, S. V., Kind, R., Oncken, O., Bock, G., Asch, G., et al. (2000). Subduction
895 and collision processes in the Central Andes constrained by converted seismic phases.
896 *Nature*, 408, 958–961. <https://doi.org/10.1038/35050073>
- 897 Zertani, S., John, T., Tilmann, F., Motra, H. B., Keppler, R., Andersen, T. B., & Labrousse, L.
898 (2019a). Modification of the seismic properties of subducting continental crust by
899 eclogitization and deformation processes. *Journal of Geophysical Research: Solid Earth*,
900 124, 9731-9754. <https://doi.org/10.1029/2019jb017741>
- 901 Zertani, S., Labrousse, L., John, T., Andersen, T. B., & Tilmann, F. (2019b). The Interplay of
902 Eclogitization and Deformation During Deep Burial of the Lower Continental Crust—A
903 Case Study From the Bergen Arcs (Western Norway). *Tectonics*, 38(3), 898-915.
904 <https://doi.org/10.1029/2018tc005297>
- 905 Zhong, X., Andersen, N. H., Dabrowski, M., & Jamtveit, B. (2019). Zircon and quartz inclusions
906 in garnet used for complementary Raman thermobarometry: application to the Holsnøy
907 eclogite, Bergen Arcs, Western Norway. *Contributions to Mineralogy and Petrology*,
908 174(6), 50. <https://doi.org/10.1007/s00410-019-1584-4>
- 909 Zhong, X., Frehner, M., Kunze, K., & Zappone, A. (2014). A novel EBSD-based finite-element
910 wave propagation model for investigating seismic anisotropy: Application to Finero
911 Peridotite, Ivrea-Verbano Zone, Northern Italy. *Geophysical Research Letters*, 41(20),
912 7105-7114. <https://doi.org/10.1002/2014GL060490>

913

914